Research
A SCIENCE PARTNER JOURNAL

RESEARCH ARTICLE

Large Spin Hall Conductivity and Excellent Hydrogen Evolution Reaction Activity in Unconventional $PtTe_{1.75}$ Monolayer

Dexi Shao[1,2], Junze Deng[1,3], Haohao Sheng[1,3], Ruihan Zhang[1,3], Hongming Weng[1,3], Zhong Fang[1,3], Xing-Qiu Chen[4,5], Yan Sun[4,5]*, and Zhijun Wang[1,3]*

[1]Beijing National Laboratory for Condensed Matter Physics, and Institute of Physics, Chinese Academy of Sciences, Beijing 100190, China. [2]Department of Physics, Hangzhou Normal University, Hangzhou 311121, China. [3]University of Chinese Academy of Sciences, Beijing 100049, China. [4]Shenyang National Laboratory for Materials Science, Institute of Metal Research, Chinese Academy of Science, Shenyang 110016, Liaoning, China. [5]School of Materials Science and Engineering, University of Science and Technology of China, Hefei, China.

*Address correspondence to: sunyan@imr.ac.cn (Y.S.); wzj@iphy.ac.cn (Z.W.)

Citation: Shao D, Deng J, Sheng H, Zhang R, Weng H, Fang Z, Chen XQ, Sun Y, Wang Z. Large Spin Hall Conductivity and Excellent Hydrogen Evolution Reaction Activity in Unconventional $PtTe_{1.75}$ Monolayer. *Research* 2023;6:Article 0042. https://doi.org/10.34133/research.0042

Submitted 6 September 2022
Accepted 16 December 2022
Published 24 February 2023

Copyright © 2023 Dexi Shao et al. Exclusive Licensee Science and Technology Review Publishing House. No claim to original U.S. Government Works. Distributed under a Creative Commons Attribution License (CC BY 4.0).

Two-dimensional (2D) materials have gained lots of attention due to the potential applications. In this work, we propose that based on first-principles calculations, the (2×2) patterned $PtTe_2$ monolayer with kagome lattice formed by the well-ordered Te vacancy ($PtTe_{1.75}$) hosts large and tunable spin Hall conductivity (SHC) and excellent hydrogen evolution reaction (HER) activity. The unconventional nature relies on the $A1 @ 1b$ band representation of the highest valence band without spin–orbit coupling (SOC). The large SHC comes from the Rashba SOC in the noncentrosymmetric structure induced by the Te vacancy. Even though it has a metallic SOC band structure, the $\mathbb{Z}_2$ invariant is well defined because of the existence of the direct bandgap and is computed to be nontrivial. The calculated SHC is as large as $1.25 \times 10^3 \frac{\hbar}{e} (\Omega\ \mathrm{cm})^{-1}$ at the Fermi level (E_F). By tuning the chemical potential from $E_F - 0.3$ to $E_F + 0.3$ eV, it varies rapidly and monotonically from -1.2×10^3 to $3.1 \times 10^3 \frac{\hbar}{e} (\Omega\ \mathrm{cm})^{-1}$. In addition, we also find that the Te vacancy in the patterned monolayer can induce excellent HER activity. Our results not only offer a new idea to search 2D materials with large SHC, i.e., by introducing inversion–symmetry breaking vacancies in large SOC systems, but also provide a feasible system with tunable SHC (by applying gate voltage) and excellent HER activity.

Introduction

In the past decade, many topological semimetals with various quasiparticle dispersions and fascinating properties have been proposed [1–5]. The layered noble transition metal dichalcogenide $PtTe_2$ is extraordinary with heavily tilted type-II Dirac fermion [6]. It hosts unique properties, such as topological nontrivial band structure [6,7], ultrahigh electrical conductivity [8,9], and robustness of the remaining semimetal phase even down to just 2 triatomic layers [10,11]. Soon after, many $PtTe_2$ derivatives have been proposed, including the monolayer, multilayer, doping, vacancy, heterojunction structures, and so on. For example, the Ir-doped $PtTe_2$ (i.e., $Pt_{1-x}Ir_xTe_2$) has realized the Fermi level (E_F) tunability and superconductivity, which opens up a new route for the investigation of Dirac physics and topological superconductivity [12–14]. More recently, $PtTe_2$-based broadband photodetectors and image sensors have been fabricated, demonstrating tremendous potential application value in various photoelectric devices [15–17]. Very recently, the patterned monolayer with kagome lattice formed by one Te vacancy in a 2×2 supercell has been grown successfully [18], whose band topology and potential properties are unknown. The study of $PtTe_2$ derivatives can not only reveal novel condensed matter physics but also facilitate the versatile development in device physics.

In this work, we theoretically propose that the recently synthesized patterned $PtTe_2$ monolayer with the Te vacancy (i.e., $PtTe_{1.75}$) hosts large spin Hall conductivity (SHC) because of the Rashba spin–orbit coupling (SOC), where the Te vacancy breaks inversion symmetry ($\boldsymbol{\mathcal{I}}$). The momentum offset and strength of the Rashba SOC are estimated, $k_0 = 0.12$ Å^{-1} and $\alpha_R = 0.8112$ eV Å. The momentum offset k_0 is very large and comparable with the largest one reported in the Bi/Ag(111) surface alloy in literature [19], which induces visible Rashba band splitting. Using the Kubo formula approach at the clean limit, we find the Rashba SOC will induce large SHC, as large as $1.25 \times 10^3 \frac{\hbar}{e} (\Omega\ \mathrm{cm})^{-1}$ at E_F. Furthermore, the SHC changes rapidly and monotonically as the chemical potential evolving

in a wide range ($E - E_F \in [-0.3,0.3]$ eV), which benefits to the potential applications in spintronics. In the end, the variation of the Gibbs free energy for hydrogen adsorption progress is considered, which indicates that the $PtTe_{1.75}$ monolayer exhibit an excellent hydrogen evolution reaction (HER) activity.

Results and Discussion

Electronic band structures

The band structures of $PtTe_{1.75}$ monolayer without and with SOC are presented in Fig. 1C and D, respectively. Comparing them, we notice that the band dispersions change dramatically. Each band splits into two nondegenerate bands in Fig. 1D. It is the Te vacancy in the monolayer that breaks $\mathcal{I}$ (and $\mathcal{TI}$), inducing the visible Rashba band splitting. From the orbital-resolved band structures in Fig. 1C, we find that there exist visible band hybridizations between Te-$p_{x,y}$ and Te-p_z orbitals around E_F. Using IRVSP [20], the irreducible representations of the high-symmetry **k** points are calculated and labeled in Fig. 2A. Accordingly, the band representation (BR) analyses indicate that the 2 conduction bands belong to E @ 1b BR, while the highest valence band belongs to $A1$ @ 1b BR, suggesting the unconventional nature of the obstructed atomic limit [21–24].

SOC often plays important roles to engineering topological states, such as quantum spin Hall effect in graphene [25,26] and $Ta_2M_3Te_5$ (M = Pd,Ni) compounds [27,28], 3D large-SOC-gap topological insulator in Bi_2Se_3 and NaCaBi families [29,30], and so on. In $PtTe_{1.75}$, once including SOC, the Te-p_z dominated band around Γ splits because of the Rashba SOC induced by the Te vacancy, as shown in Fig. 1D. To get more insights in the nontrivial band topology and Rashba SOC band splitting, we have explored how the band structure evolves with the increasing strength of SOC (denoted by λ) gradually in Fig. 2. We notice that the nontrivial band topology for $N_e - 4$ occupied bands is due to the SOC (can be infinitesimal)-induced bandgap at Γ without involving band inversion [31,32]. In addition, the nontrivial topologies for $N_e - 2$ and N_e occupied bands are due to a gap closing and reopening process as varing λ. Taking $N_e - 2$ occupied bands as an example, the critical Weyl band crossing between the $(N_e - 2)$th band and the $(N_e - 1)$th band appears on the M–K line with $\lambda = 0.8$, as highlighted by a red dashed ring in Fig. 2E. Similarly, the critical Weyl point (WP) between the N_eth band and the $(N_e + 1)$th band appears on the K–Γ line with $\lambda = 0.98$, as the right inset shown in Fig. 2F. However, it becomes topologically trivial for $N_e + 2$ occupied bands because there are 2 nontrivial gap openings around both Γ and M.

Because of the existence of R_{3z} and M_{100} symmetries, the critical WPs abovementioned appear in sextuplet in the first BZ, as shown in Fig. 3A and B. Similar with WPs in 3D Weyl semimetals [33–36], these critical WPs also conform to the codimensional analysis. This can be deduced as follows. First, both the M–K ($k_y = \pi$) and K–Γ ($k_y = 0$) lines are $M_{100} * T$ invariant. In the 2-band $\boldsymbol{k} \cdot \boldsymbol{p}$ Hamiltonian depicting the Weyl band crossing, the combined antiunitary symmetry with $[TM_{100}]^2 = 1$ will reduce the number of the independent σ matrices in the $\boldsymbol{k} \cdot \boldsymbol{p}$ Hamiltonian to 2. Second, the k_x value in both the TM_{100} invariant lines and the SOC strength λ are 2 tunable parameters to search a WP. Thus, the number of the independent σ matrices in the $\boldsymbol{k} \cdot \boldsymbol{p}$ Hamiltonian equals to the number of the tunable parameters, which indicates that a WP is stable in the 2D parameter space $\{k_x, \lambda\}$. In other words, a topological phase transition can happen by tuning λ in the $M_{100} * T$ invariant lines. Through the gap closing and reopening process in the evolution, it becomes topologically nontrivial for N_e ($N_e - 2$) occupied bands. As a result, we can expect the existence of the helical edge states of the patterned $PtTe_2$ monolayer. The edge spectra are presented in Fig. S3B and D (in Section C of the SM).

Rashba SOC at Γ

Because the Te vacancy breaks $\mathcal{I}$ in the patterned $PtTe_2$ monolayer, the Rashba SOC band splitting will appear inevitably. As the projected band structures shown in Fig. 3C, the Te-p_z dominated parabolic bands splits clearly near Γ. The splitting bands near Γ can be well fitted by $E = \frac{[\hbar(k \pm k_0)]^2}{2M}$ with $M = 2.02659\ m_e$ (m_e denoting the free electronic mass) and $k_0 = 0.12$ Å^{-1} (the momentum offset), as the 2 blue parabolas shown in Fig. 3C. The coupling strength of the Rashba SOC can be derived as $\alpha_R = \frac{2E_R}{k_0} = \frac{\hbar^2 k_0}{M} = 0.81$ eVÅ. The estimated k_0 is super large in Fig. 3C, as large as the the Bi/Ag(111) surface alloy [19].

Large SHC effect

To explore the intrinsic SHC in the patterned $PtTe_2$ monolayer, the Wannier-based TB model under bases of the Te-p and Pt-d orbitals is extracted from the DFT calculations. As shown in

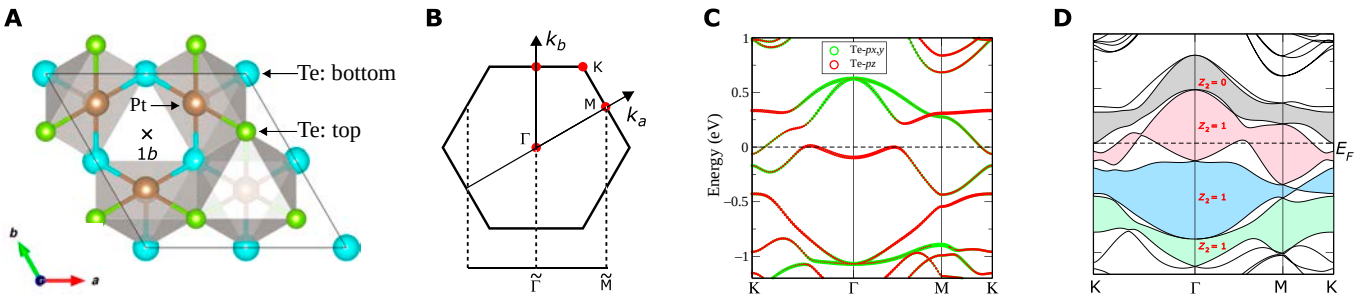


Fig. 1. (Color online) (A)Crystal structure of the patterned $PtTe_2$ monolayer ($PtTe_{1.75}$). The pristine $PtTe_2$ monolayer system in the kagome lattice contains 2 Te layers, with 4 Te atoms in both the bottom layer and the top layer of the (2 × 2) supercell. In addition, the $PtTe_{1.75}$ system comes from the patterned $PtTe_2$ monolayer with a well-ordered Te vacancy (schematized by "×" at the 1b Wyckoff site) at the top layer of the (2 × 2) supercell. Thus, there are 3 Te atoms (denoted by green ball) occupying the top layer, while there are 4 Te atoms (denoted by blue ball) occupying the bottom layer in the $PtTe_{1.75}$ system. (B) The corresponding 2D bulk BZ and 1-dimensional projected BZ orthogonal to the (01) edge. Band structures of the $PtTe_{1.75}$ system (C) without and (D) with SOC. The light green, blue, red, and gray zones in (D) indicate that there exist direct bandgaps between the corresponding adjacent bands. Thus, the time reversal $\mathbb{Z}_2$ can be defined and calculated to be 1, 1, 1, and 0 with ($N_e - 4$), ($N_e - 2$), N_e, and ($N_e + 2$) occupied bands.

Fig. S2A and B, the fitted Wannier-based TB bands can reproduce the DFT bands perfectly. On the basis of this Wannier-based TB model, we have employed the Kubo formula approach at the clean limit [37–41] to calculate the SHC of the patterned $PtTe_2$ monolayer,

$$\sigma^{\gamma}_{\alpha\beta} = \frac{e}{\hbar}\sum_{n}\int_{BZ}\frac{d\mathbf{k}}{(2\pi)^2} f_n(\mathbf{k})\Omega^{\gamma}_{\alpha\beta;n}(\mathbf{k}),$$

$$\Omega^{\gamma}_{\alpha\beta;n}(\mathbf{k}) = 2i\hbar^2\sum_{m\neq n}\frac{\left\langle u^n_{\mathbf{k}}|\hat{J}^{\gamma}_{\alpha}|u^m_{\mathbf{k}}\right\rangle\left\langle u^m_{\mathbf{k}}|\hat{v}_{\beta}|u^n_{\mathbf{k}}\right\rangle}{\left(\varepsilon^n_{\mathbf{k}}-\varepsilon^m_{\mathbf{k}}\right)^2}, \quad (1)$$

where $\hat{J}^{\gamma}_{\alpha} = \frac{1}{2}\{\hat{v}_{\alpha},\hat{s}_{\gamma}\}$ is the spin current operator, with $\hat{s}$ denoting the spin operator, $\hat{v}_{\alpha} = \frac{\partial\hat{H}}{\hbar\partial k_{\alpha}}$ denoting the velocity operator, and $\alpha,\beta,\gamma = \{x,y,z\}$. $f_n(\mathbf{k})$ is the Fermi–Dirac distribution. $|u^n_{\mathbf{k}}\rangle$ and $\varepsilon^n_{\mathbf{k}}$ are the eigenvectors and eigenvalues of the TB Hamiltonian, respectively. The distributions of $\mathcal{O}_N(\mathbf{k}) \equiv \sum_{n=1}^{N}\Omega^{x}_{yz;n}(\mathbf{k})$ for $N = N_e - 1$ and N_e occupied bands are presented in Fig. 3D and E, respectively. As the calculated SHC as a function of the chemical potential shown in Fig. 3G, one can find that the calculated SHC is as large as $1.25\times10^3\frac{\hbar}{e}(\Omega\ \mathrm{cm})^{-1}$ at $E = E_F$. The corresponding distribution at $E = E_F$ is presented in Fig. 3F, which indicates that the large contribution of the SHC at K comes from the SOC band splitting. In addition, the SHC changes rapidly and monotonically in a wide energy window ranging from $E_F - 0.3$ eV to $E_F + 0.3$ eV. At $E - E_F = -0.3$ eV, the SHC changes the sign and becomes $-1.2\times10^3\frac{\hbar}{e}(\Omega\ \mathrm{cm})^{-1}$, while at $E - E_F = 0.3$ eV, the SHC nearly triples and becomes $3.1\times10^3\frac{\hbar}{e}(\Omega\ \mathrm{cm})^{-1}$. In general, the chemical potential can be tuned by applying gate voltage or introducing chemical doping at the vacancy. As shown in Fig. S5A to C, we can find that the absorption of Tl/Pb at the vacancy behaves as electron dopings, which will increase the E_F with negligible changes in the band structure. We think our results will be benefitial to the potential applications in spintronics.

Excellent HER activity

According to the new principle for active catalytic sites [23,42,43], the obstructed bulk states in the patterned monolayer (which can be seen as the limit of obstructed surface states) may bring measured catalytic activity. By exposing undercoordinated atoms as the active sites, vacancy engineering is an important strategy to optimize the HER performance of the basal planes in 2D materials [44,45]. As the acidic HER of the $PtTe_{1.75}$ is schematized in Fig. 4A, protons (H^+) in solution generate adsorbed H atoms (H^*) as intermediate and then the H atoms on the catalyst surface are desorbed to produce hydrogen (H_2), which can be formulized as

$$H^+ + e^- + * \rightarrow H^* \rightarrow \frac{1}{2}H_2 + *. \quad (2)$$

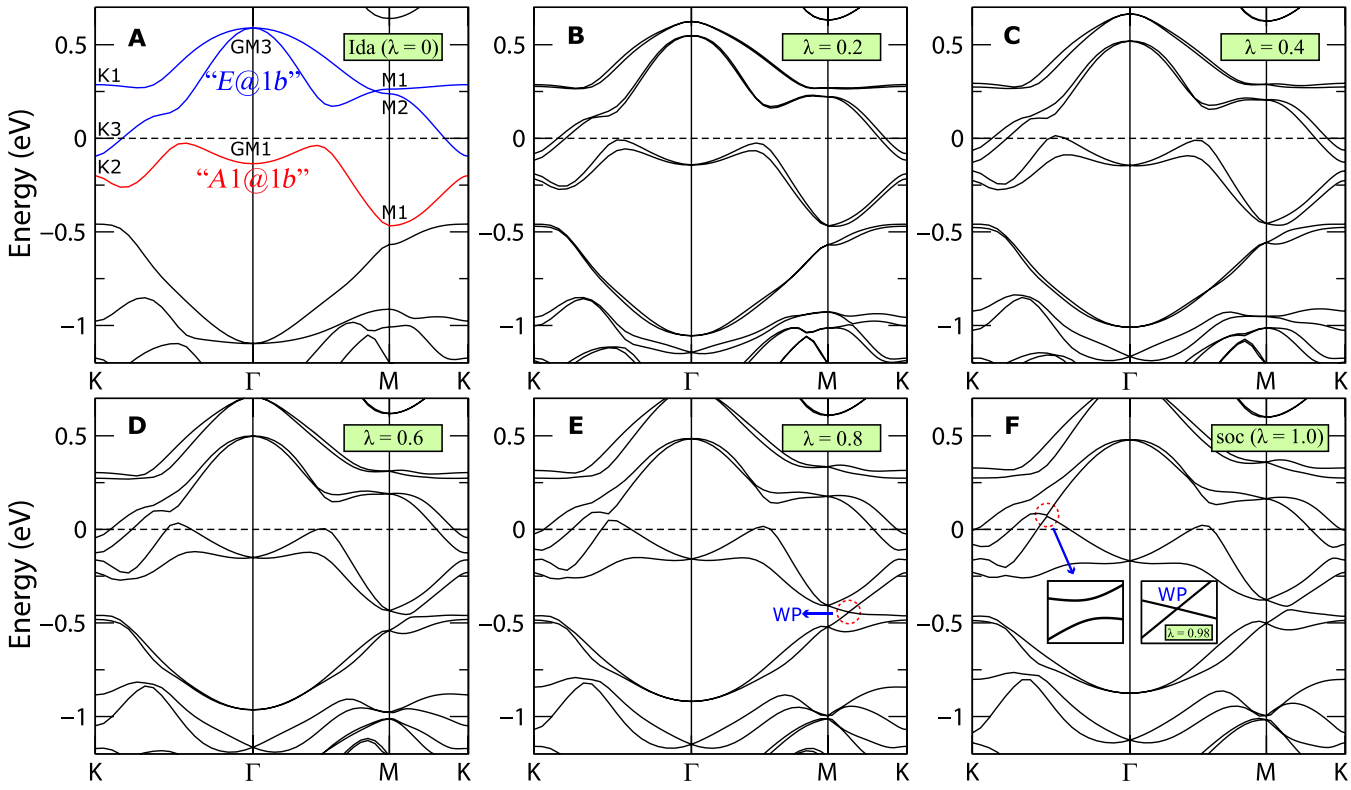


Fig. 2. (Color online) Band structures of $PtTe_{1.75}$ monolayer with the strength of SOC (A) $\lambda = 0$ (without SOC), (B) $\lambda = 0.2$, (C) $\lambda = 0.4$, (D) $\lambda = 0.6$, (E) $\lambda = 0.8$, and (F) $\lambda = 1.0$ (with actual SOC). For the case without SOC shown in (A), the 2 conduction bands schematized by 2 blue lines belong to *E*@1*b* BR, while the highest valence band schematized by the red line belongs to *A*1@1*b* BR. There exists a WP along the M–K line below E_F when $\lambda = 0.8$. Bands near E_F undergoes a gap closing and reopening progress when the strength of SOC evolves from 0.0 to 1.0, which gives a topological nontrivial bandgap with SOC ($\lambda = 1.0$). The critical transition occurs at $\lambda = 0.98$ (right inset in the $\lambda = 1.0$ panel), which gives another WP along the K–Γ line.

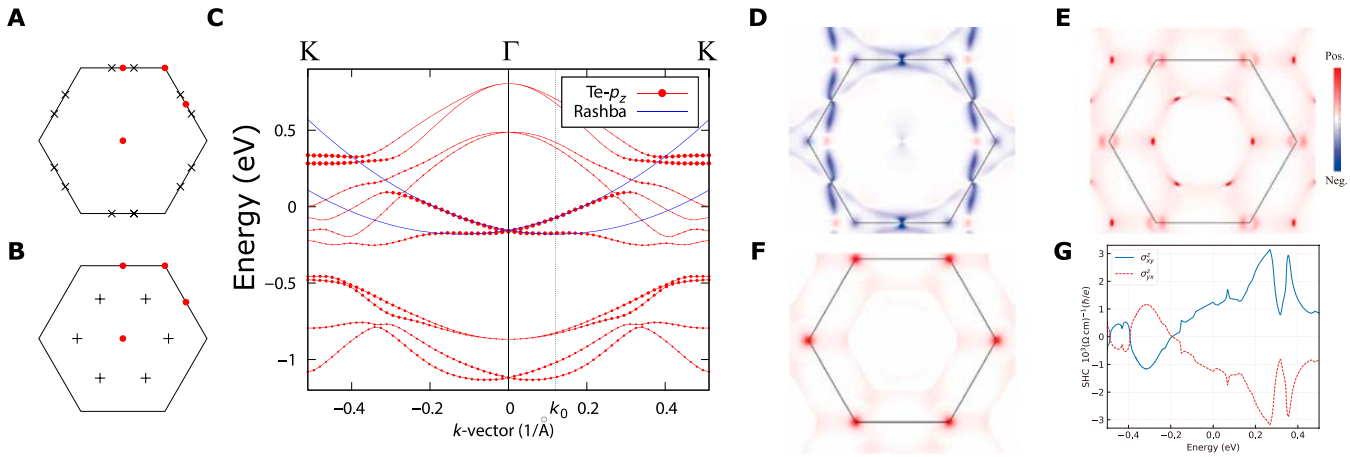


Fig. 3. (Color online) The 6 symmetry-related (R_{3z} and M_{100}) WPs formed by band crossings (A) between the (N_e-2)th band and the (N_e-1)th band with $\lambda=0.8$ as well as (B) the N_eth band and the (N_e+1)th band with $\lambda=0.98$. (C) The Te-p_z projected band structures with SOC, and the 2 blue lines depict the parabolically asymptotic behavior of the Rashba SOC induced splitting bands near the Γ point. The distribution of (D) $\mathcal{O}_{N_e-1}(\mathbf{k})$ and (E) $\mathcal{O}_{N_e}(\mathbf{k})$ in the 2D BZ. (F) The distribution of σ^z_{xy} at E_F. (G) The calculated SHC vs. the chemical potential (ranging from $E_F-0.5$ eV to $E_F+0.5$ eV).

Here "*" denotes some site on the surface, i.e., a "*" by itself denotes a free site, while H* denotes a hydrogen atom absorbed on the surface. Te vacancy-induced states near E_F give $PtTe_{1.75}$ monolayer larger electrical conductivity than pristine $PtTe_2$ monolayer, which will effectively facilitate electron transfer for HER. We used a 2×2 $PtTe_{1.75}$ supercell to simulate the basal plane. Compared with the fully coordinated Te atoms, H atoms are more likely to be adsorbed near the undercoordinated Pt atoms, just as the most stable and metastable structures shown in Fig. 4B and C. Details of screening stable adsorption sites can be found in the SM. It is well known that the change of Gibbs free energy induced by hydrogen adsorption (ΔG_{H^*}) is an important descriptor of HER activity [46–48], and an ideal catalyst for HER should host a near-zero ΔG_{H^*}, which can effectively maintain the balance between adsorption and desorption steps [47]. As shown in Fig. 4D, unlike the pristine $PtTe_2$ monolayer with a large positive ΔG_{H^*} due to its extremely inert basal plane, the $PtTe_{1.75}$ monolayer hosts an optimal ΔG_{H^*} (0.08 eV), which is slightly superior to the benchmark material Pt ($\Delta G_{H^*}=-0.09$ eV) [46]. Details of the free energy correction can be found in the SM. Here, we noted that the effect of the size on the ΔG_{H^*} is negligible, which can be deduced from Table S2. Thus, the active Pt sites induced by Te vacancy greatly optimize hydrogen adsorption in the intermediate, which will significantly improve HER performance [49]. According to Nørskov *et al.* [46], the theoretical exchange current density (i_0) as a function of ΔG_{H^*} is calculated. As shown in Fig. 4E, the $PtTe_{1.75}$ monolayer approaches the volcanic peak from the right with $i_0=0.68$ mA cm^{-2}, which is comparable to commercial Pt/C catalyst ($i_0=1.2$ mA cm^{-2}) [50]. In addition, as shown in Fig. S4A and B, the energy pathways and corresponding energy barriers of the (a) Heyrovsky and (b) Tafel reactions to release hydrogen in HER are exhibited, from which we can find that the Tafel reactions to release hydrogen is preferred. Therefore, Te vacancy can greatly stimulate the catalytic activity of $PtTe_2$ basal plane and produce excellent HER performance.

Conclusion

We find that the $PtTe_{1.75}$ not only hosts the unique band structure with 3 lower-energy bands belonging to $(A1+E)$ @ $1b$ BRs at an empty site but also exhibits large and tunable SHC and excellent HER performance. First, we have calculated the time reversal invariant $\mathbb{Z}_2$, which indicates the 2D topological insulator nature in the patterned $PtTe_2$ monolayer. We demonstrate that the topological phase can be deduced by a gap closing and reopening process with the evolution of the strength of SOC from $\lambda=0$ to $\lambda=1.0$. The critical phase transition occurs at $\lambda=0.98$, which gives a sextuplet of critical WPs. Second, the Te vacancy breaks $\mathcal{I}$ and induces Rashba SOC band splitting. The estimated momentum offset is super large with $k_0=0.12$ Å^{-1}. Third, we find that the SHC is as large as $1.25\times10^3\frac{\hbar}{e}(\Omega\text{ cm})^{-1}$ at E_F. Furthermore, the SHC varies quickly and almost monotonically from -1.2 to $3.1\times10^3\frac{\hbar}{e}(\Omega\text{ cm})^{-1}$, indicating that the SHC in the patterned $PtTe_2$ monolayer can be conveniently tuned for various applications. Last, we also find the Te vacancy in the patterned monolayer can induce excellent HER activity. These results not only offer a new idea to search 2D materials with large SHC, i.e., by introducing inversion–symmetry breaking vacancies in large SOC systems, but also provide a feasible system for the potential application in spintronics and HER catalysts.

Materials and Methods

The pristine $PtTe_2$ crystallizes in the CdI_2-type trigonal ($1T$) structure with $P\bar{3}m1$ space group (SG). It hosts the layered structure stacking along the z axis and can be easily tuned by strain, which indicates that it can be grown under various substrates. The patterned monolayer with kagome lattice formed by one Te vacancy in the 2×2 supercell has been successfully grown on the Pt(111) surface [18]. As shown in Fig. 1A, the patterned $PtTe_2$ monolayer contains 2 Te layers: 4 Te atoms (blue balls) in the bottom layer and 3 Te atoms (green balls; with one vacancy schematized by "×" at $1b$ Wyckoff site) in the top layer. The distance between the bottom and top layers is $d_0=2.7253$ Å. The Te vacancy breaks $\mathcal{I}$, resulting in a noncentrosymmetrical structure with the p3m1 layer group (LG 69; corresponding to SG $P\bar{3}m1$ excluding translational symmetry along the z axis). Thus, the Rashba SOC-induced band splitting is inevitable. The lattice parameters and atomic positions are listed in Table S1 of the Supplementary Materials (SM).

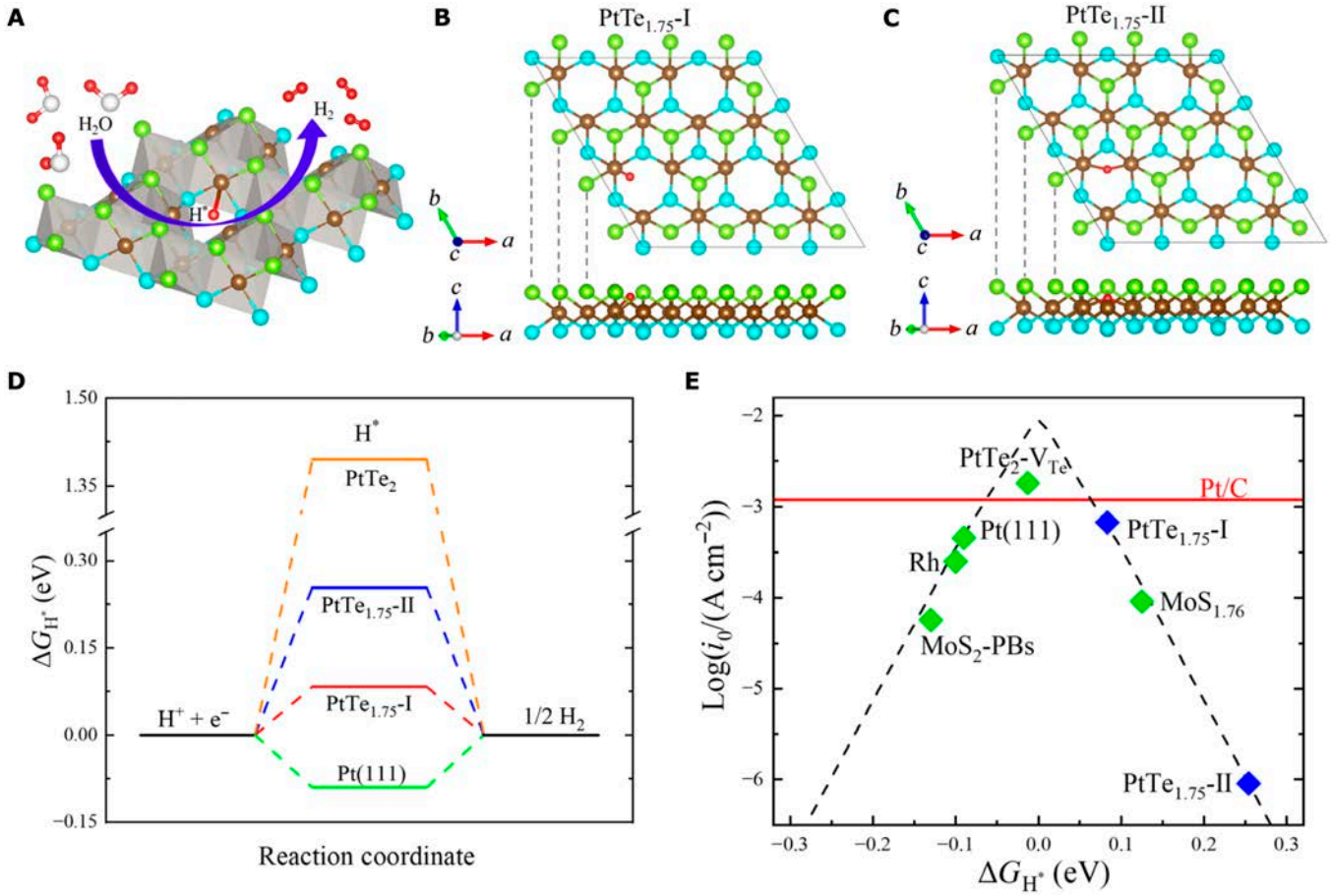


Fig. 4. (Color online) (A) Schematic diagram of HER process on $PtTe_{1.75}$ monolayer. Top and side views of (B) the most stable ($PtTe_{1.75}$-I) and (C) metastable ($PtTe_{1.75}$-II) structures after H atom adsorption. The red ball denotes the absorbed H atom. (D) Variation of the Gibbs free energy for hydrogen adsorption (ΔG_{H^*}) to different compounds. (E) Volcano plot depicting the relationship between exchange current density (i_0) and ΔG_{H^*}, in which cases of Pt(111) [46], Rh [46], Pt/C [50], $PtTe_2$ with ordered trigonal Te vacancies ($PtTe_2$-V_{Te}) [44], $MoS_{1.76}$ [45], and 2H-1T phase boundaries of MoS_2 (MoS_2-PBs) [51] are also included for comparison.

We performed the first-principles calculations based on the density functional theory (DFT) using projector augmented wave method [52,53] implemented in the Vienna ab initio simulation package (VASP) [54,55]. The generalized gradient approximation with exchange–correlation functional of Perdew, Burke, and Ernzerhof for the exchange–correlation functional [56] was adopted. The kinetic energy cutoff was set to 500 eV for the plane wave bases. The thickness of the vacuum layer along z axis was set to >20 Å. The brillouin zone (BZ) was sampled by Γ-centered Monkhorst–Pack method with a 12 × 12 × 1 **k**-mesh for the 2-dimensional (2D) periodic boundary conditions in the self-consistent process. The Wilson loop technique [57] was used to calculate the $\mathbb{Z}_2$ topological invariant. In addition, the electronic structures near E_F were doubly checked by the full-potential local-orbital code [58] and fully consistent with those from VASP. To compute SHC, a Wannier-based tight-binding (TB) model under bases of the Te-p and Pt-d orbitals is extracted from the DFT calculations.

Acknowledgments

Funding: This work was supported by the National Natural Science Foundation of China (grant no. 12204138, no. 11974395, no. 12188101, no. 52188101, and no. 51725103), the Strategic Priority Research Program of Chinese Academy of Sciences (grant no. XDB33000000), and the Center for Materials Genome.
Competing interests: The authors declare that they have no competing interests.

Data Availability

The datasets used in this article are available from the corresponding author upon request.

Supplementary Materials

Section A. Lattice parameters of the patterned $PtTe_2$ monolayer with a Te vacancy.
Section B. The calculated weak topological invariant Z_2.
Section C. Topological surface states of the patterned $PtTe_2$ monolayer.
Section D. Releasing hydrogen in HER.
Section E. Screening adsorption sites and the correction of Gibbs free energy.
Section F. Band structures vs. dopping.
Table S1. Crystal structures of the patterned $PtTe_2$ monolayer in terms of SG $P3m1$ (SG 156).
Table S2. The Gibbs free energy correction terms of the most thermodynamically stable $PtTe_{1.75}$ adsorption structures with

1×1, 2×2, 3×3, and 4×4 supercell, including adsorption energies of hydrogen (ΔE_H*), the change of zero-point energy (ΔZPE), enthalpy correction ($\Delta \int C_p dT$), entropy correction (ΔTS), and Gibbs free energy (ΔG_H*).
Fig. S1. (Color online) The calculated weak topological invariant Z_2 for (A) 80, (B) 82, (C) 84, and (D) 86 occupied bands, respectively.
Fig. S2. (Color online) DFT vs. Wannier bands (A) without SOC and (B) with SOC.
Fig. S3. (Color online) The projected edge states along (01) direction (A) without SOC and (B) with SOC in the upper edge.
Fig. S4. (Color online) Energy pathways of the (A) Heyrovsky and (B) Tafel reactions on $PtTe_{1.75}$ monolayer to release hydrogen.
Fig. S5. (Color online) Band structures of the patterned $PtTe_2$ monolayer with (A) no doping (Te vacancy), (B) Tl doping, and (C) Pb doping at the Te vacancy position.
References [59–62]

References

1. Armitage NP, Mele EJ, Vishwanath A. Weyl and Dirac semimetals in three-dimensional solids. *Rev Mod Phys*. 2018;90(1):Article 015001.
2. Wan X, Turner AM, Vishwanath A, Savrasov SY. Topological semimetal and Fermi-arc surface states in the electronic structure of pyrochlore iridates. *Phys Rev B*. 2011;83(20):Article 205101.
3. Wang Z, Weng H, Wu Q, Dai X, Fang Z. Three-dimensional Dirac semimetal and quantum transport in Cd_3As_2. *Phys Rev B*. 2013;88(12):Article 125427.
4. Bradlyn B, Cano J, Wang Z, Vergniory MG, Felser C, Cava RJ, Bernevig BA. Beyond Dirac and Weyl fermions: Unconventional quasiparticles in conventional crystals. *Science*. 2016;353(6299):Article aaf5037.
5. Wieder BJ, Kim Y, Rappe AM, Kane CL. Double Dirac semimetals in three dimensions. *Phys Rev Lett*. 2016;116(18):Article 186402.
6. Yan M, Huang H, Zhang K, Wang E, Yao W, Deng K, Wan G, Zhang H, Arita M, Yang H, et al. Lorentz-violating type-II Dirac fermions in transition metal dichalcogenide $PtTe_2$. *Nat Commun*. 2017;8:257.
7. Politano A, Chiarello G, Ghosh B, Sadhukhan K, Kuo C-N, Lue CS, Pellegrini V, Agarwal A. 3D Dirac plasmons in the type-II Dirac semimetal $PtTe_2$. *Phys Rev Lett*. 2018;121(8):Article 086804.
8. Fu L, Hu D, Mendes RG, Rummeli MH, Dai Q, Wu B, Liu Y. Highly organized epitaxy of Dirac semimetallic $PtTe_2$ crystals with extrahigh conductivity and visible surface plasmons at edges. *ACS Nano*. 2018;12(9):9405–9411.
9. Hao S, Zeng J, Xu T, Cong X, Wang C, Wu C, Wang Y, Liu X, Cao T, Su G, et al. Low-temperature eutectic synthesis of $PtTe_2$ with weak antilocalization and controlled layer thinning. *Adv Funct Mater*. 2018;28(36):Article 1803746.
10. Lin M-K, Villaos RAB, Hlevyack JA, Chen P, Liu R-Y, Hsu C-H, Avila J, Mo S-K, Chuang F-C, Chiang T-C. Dimensionality-mediated semimetal-semiconductor transition in ultrathin $PtTe_2$ films. *Phys Rev Lett*. 2020;124(3):Article 036402.
11. Deng K, Yan M, Yu C-P, Li J, Zhou X, Zhang K, Zhao Y, Miyamoto K, Okuda T, Duan W, et al. Crossover from 2D metal to 3D Dirac semimetal in metallic $PtTe_2$ films with local Rashba effect. *Sci Bull*. 2019;64(15):1044–1048.
12. Fei F, Bo X, Wang P, Ying J, Li J, Chen K, Dai Q, Chen B, Sun Z, Zhang M, et al. Band structure perfection and superconductivity in type-II Dirac semimetal $Ir_{1-x}Pt_xTe_2$. *Adv Mater*. 2018;30(35):Article 1801556.
13. Jiang J, Lee S, Fei F, Song F, Vescovo E, Kaznatcheev K, Walker FJ, Ahn CH. A comprehensive ARPES study on the type-II Dirac semimetal candidate $Ir_{1-x}Pt_xTe_2$. *APL Mater*. 2020;8:Article 061106.
14. Nie S, Xing L, Jin R, Xie W, Wang Z, Prinz FB. Topological phases in the $TaSe_3$ compound. *Phys Rev B*. 2018;98(12):Article 125143.
15. Tong X-W, Lin Y-N, Huang R, Zhang Z-X, Fu C, Wu D, Luo L-B, Li Z-J, Liang F-X, Zhang W. Direct tellurization of Pt to synthesize 2D $PtTe_2$ for high-performance broadband photodetectors and NIR image sensors. *ACS Appl Mater Interfaces*. 2020;12(48):53921–53931.
16. Shawkat MS, Hafiz SB, Islam MM, Mofid SA, Al Mahfuz MM, Biswas A, Chung H-S, Okogbue E, Ko T-J, Chanda D, et al. Scalable Van der Waals two-dimensional $PtTe_2$ layers integrated onto silicon for efficient near-to-mid infrared photodetection. *ACS Appl Mater Interfaces*. 2021;13(13):15542–15550.
17. Xu H, Guo C, Zhang J, Guo W, Kuo C-N, Lue CS, Hu W, Wang L, Chen G, Politano A, et al. $PtTe_2$-based type-II Dirac semimetal and its van der Waals heterostructure for sensitive room temperature terahertz photodetection. *Small*. 15(52):Article 1903362.
18. Liu L, Zemlyanov D, Chen YP. Epitaxial growth of monolayer $PdTe_2$ and patterned $PtTe_2$ by direct tellurization of Pd and Pt surfaces. *2D Mater*. 2021;8:Article 045033.
19. Ast CR, Henk J, Ernst A, Moreschini L, Falub MC, Pacilé D, Bruno P, Kern K, Grioni M. Giant spin splitting through surface alloying. *Phys Rev Lett*. 2007;98(18):Article 186807.
20. Blöchl PE. Projector augmented-wave method. *Phys Rev B*. 1994;50(24):17953–17979.
21. Kresse G, Joubert D. From ultrasoft pseudopotentials to the projector augmented-wave method. *Phys Rev B*. 1999;59(3):1758–1775.
22. Kresse G, Furthmüller J. Efficiency of ab-initio total energy calculations for metals and semiconductors using a plane-wave basis set. *Comput Mater Sci*. 1996;6(1):15–50.
23. Kresse G, Furthmüller J. Efficient iterative schemes for *ab initio* total-energy calculations using a plane-wave basis set. *Phys Rev B*. 1996;54(16):11169–11186.
24. Perdew JP, Burke K, Ernzerhof M. Generalized gradient approximation made simple. *Phys Rev Lett*. 1996;77(18):3865–3868.
25. Yu R, Qi XL, Bernevig A, Fang Z, Dai X. Equivalent expression of $\mathbb{Z}_2$ topological invariant for band insulators using the non-Abelian Berry connection. *Phys Rev B*. 2011;84(7):Article 075119.
26. Koepernik K, Eschrig H. Full-potential nonorthogonal local-orbital minimum-basis band-structure scheme. *Phys Rev B*. 1999;59(3):1743–1757.
27. Gao J, Wu Q, Persson C, Wang Z. Irvsp: To obtain irreducible representations of electronic states in the VASP. *Comput Phys Commun*. 2021;261:Article 107760.
28. Nie S, Qian Y, Gao J, Fang Z, Weng H, Wang Z. Application of topological quantum chemistry in electrides. *Phys Rev B*. 2021;103(20):Article 205133.
29. Nie S, Bernevig BA, Wang Z. Sixfold excitations in electrides. *Phys Rev Res*. 2021;3(1):Article L012028.
30. Gao J, Qian Y, Jia H, Guo Z, Fang Z, Liu M, Weng H, Wang Z. Unconventional materials: The mismatch between electronic charge centers and atomic positions. *Sci Bull*. 2022;67(6):598–608.

31. Xu Y, Elcoro L, Song Z-D, Vergniory MG, Felser C, Parkin SSP, Regnault N, Manes JL, Bernevig BA. Filling-enforced obstructed atomic insulators. arXiv. 2021. https://arxiv.org/abs/2106.10276.
32. Kane CL, Mele EJ. Z_2 topological order and the quantum spin Hall effect. *Phys Rev Lett*. 2005;95(14):Article 146802.
33. Kane CL, Mele EJ. Quantum spin Hall effect in graphene. *Phys Rev Lett*. 2005;95(22):226801.
34. Guo Z, Yan D, Sheng H, Nie S, Shi Y, Wang Z. Quantum spin Hall effect in $Ta_2 M_3 Te_5$ (M = Pd, Ni). *Phys Rev B*. 2021;103(11):Article 115145.
35. Wang X, Geng D, Yan D, Hu W, Zhang H, Yue S, Sun Z, Kumar S, Schwier EF, Shimada K, et al. Observation of topological edge states in the quantum spin Hall insulator $Ta_2Pd_3Te_5$. *Phys Rev B*. 2021;104(24):Article L241408.
36. Zhang H, Liu C-X, Qi X-L, Dai X, Fang Z, Zhang S-C. Topological insulators in Bi_2Se_3, Bi_2Te_3 and Sb_2Te_3 with a single Dirac cone on the surface. *Nat Phys*. 2009;5:438–442.
37. Shao D, Guo Z, Wu X, Nie S, Sun J, Weng H, Wang Z. Topological insulators in the NaCaBi family with large spin-orbit coupling gaps. *Phys Rev Res*. 2021;3(1):Article 013278.
38. Bradlyn B, Elcoro L, Cano J, Vergniory MG, Wang Z, Felser C, Aroyo MI, Bernevig BA. Topological quantum chemistry. *Nature*. 2017;547:298–305.
39. Deng J, Shao D, Gao J, Yue C, Weng H, Fang Z, Wang Z. Twisted nodal wires and three-dimensional quantum spin Hall effect in distorted square-net compounds. *Phys Rev B*. 2022;105(22):Article 224103.
40. Qian Y, Gao J, Song Z, Nie S, Wang Z, Weng H, Fang Z. Weyl semimetals with S_4 symmetry. *Phys Rev B*. 2020;101(15):Article 155143.
41. Gao J, Qian Y, Nie S, Fang Z, Weng H, Wang Z. High-throughput screening for Weyl semimetals with S_4 symmetry. *Sci Bull*. 2021;66(7):667–675.
42. Nie S, Sun Y, Prinz FB, Wang Z, Weng H, Fang Z, Dai X. Magnetic semimetals and quantized anomalous Hall effect in EuB_6. *Phys Rev Lett*. 2020;124(7):Article 076403.
43. Shi W, Wieder BJ, Meyerheim HL, Sun Y, Zhang Y, Li Y, Shen L, Qi Y, Yang L, Jena J, et al. A charge-density-wave topological semimetal. *Nat Phys*. 2021;17(3):381–387.
44. Zhang Y, Sun Y, Yang H, Železný JZ, Parkin SPP, Felser C, Yan B. Strong anisotropic anomalous Hall effect and spin Hall effect in the chiral antiferromagnetic compounds $Mn_3 X$ (X = Ge, Sn, Ga, Ir, Rh, and Pt). *Phys Rev B*. 2017;95(7):Article 075128.
45. Xiao D, Chang M-C, Niu Q. Berry phase effects on electronic properties. *Rev Mod Phys*. 2010;82(3):1959–2007.
46. King-Smith RD, Vanderbilt D. Theory of polarization of crystalline solids. *Phys Rev B*. 1993;47(3):1651–1654.
47. Vanderbilt D, King-Smith RD. Electric polarization as a bulk quantity and its relation to surface charge. *Phys Rev B*. 1993;48(7):4442–4455.
48. Vanderbilt D. *Berry phases in electronic structure theory: Electric polarization, orbital magnetization and topological insulators*. Cambridge (UK): Cambridge University Press; 2018.
49. Xu Y, Elcoro L, Li G, Song Z-D, Regnault N, Yang Q, Sun Y, Parkin S, Felser C, Bernevig BA. Three-dimensional real space invariants, obstructed atomic insulators and a new principle for active catalytic sites. arXiv. 2021. https://arxiv.org/abs/2111.02433.
50. Li G, Xu Y, Song Z, Yang Q, Gupta U, Süβ V, Sun Y, Sessi P, Parkin SSP, Bernevig BA, et al. Obstructed surface states as the origin of catalytic activity in inorganic heterogeneous catalysts. arXiv. 2021. https://arxiv.org/abs/2111.02435.
51. Li X, Fang Y, Wang J, Fang H, Xi S, Zhao X, Xu D, Xu H, Yu W, Hai X, et al. Ordered clustering of single atomic Te vacancies in atomically thin $PtTe_2$ promotes hydrogen evolution catalysis. *Nat Commun*. 2021;12:2351.
52. Jiang L, Zhou Q, Li J-J, Xia Y-X, Li H-X, Li Y-J. Engineering isolated S vacancies over 2D MoS_2 basal planes for catalytic hydrogen evolution. *Appl ACS Nano Mater*. 2022;5(3):3521–3530.
53. Nørskov JK, Bligaard T, Logadottir A, Kitchin JR, Chen JG, Pandelov S, Stimming U. Trends in the exchange current for hydrogen evolution. *J Electrochem Soc*. 2005;152(2):J23–J26.
54. Greeley J, Jaramillo TF, Bonde J, Chorkendorff I, Nørskov JK. Computational high-throughput screening of electrocatalytic materials for hydrogen evolution. *Nat Mater*. 2006;5(11):909–913.
55. Nørskov JK, Rossmeisl J, Logadottir A, Lindqvist L, Kitchin JR, Bligaard T, Jonsson H. Origin of the overpotential for oxygen reduction at a fuel-cell cathode. *J Phys Chem B*. 2004;108(46):17886–17892.
56. Lei B, Zhang YY, Du SX. Prediction of structured void-containing 1T-$PtTe_2$ monolayer with potential catalytic activity for hydrogen evolution reaction. *Chin Phys B*. 2021;29(5):Article 058104.
57. Yang Q, Li G, Zhang Y, Liu J, Rao J, Heine T, Felser C, Sun Y. Transition metal on topological chiral semimetal PdGa with tailored hydrogen adsorption and reduction. *Npj Comput Mater*. 2021;7:207.
58. Zhu J, Wang Z-C, Dai H, Wang Q, Yang R, Yu H, Liao M, Zhang J, Chen W, Wei Z, et al. Boundary activated hydrogen evolution reaction on monolayer MoS_2. *Nat Commun*. 2019;10:1348.
59. Sancho MPL, Sancho JML, Sancho JML, Rubio J. Highly convergent schemes for the calculation of bulk and surface Green functions. *J Phys F*. 1985;15(4):851.
60. Marzari N, Mostofi AA, Yates JR, Souza I, Vanderbilt D. Maximally localized Wannier functions: Theory and applications. *Rev Mod Phys*. 2012;84(4):1419–1475.
61. Wu Q, Zhang S, Song H-F, Troyer M, Soluyanov AA. WannierTools: An open-source software package for novel topological materials. *Comput Phys Commun*. 2018;224:405–416.
62. Henkelman G, Uberuaga BP, Jónsson H. A climbing image nudged elastic band method for finding saddle points and minimum energy paths. *J Chem Phys*. 2000;113:9901.